Journal of Cluster Science (2023) 34:881–892
https://doi.org/10.1007/s10876-022-02266-x

ORIGINAL PAPER

Synthesis, Crystal Structures, Photoluminescence and Magnetic Properties of Lanthanide(III) Complexes Based on 2-(Thiophen-2-ylselanyl)acetic Acid Ligand

Jing Wang[1] · Fan Zhang[2] · Ru-Fen Zhang[1] · Jing Ru[1] · Qian-Li Li[1] · Xiu-mei Du[1] · Chun-Lin Ma[1]

Received: 5 February 2022 / Accepted: 6 April 2022 / Published online: 25 April 2022

Abstract

Six dinuclear lanthanide(III) complexes $[Ln_2(L)_6(phen)_2]$ (Ln = Eu^{III} (**1**), Tb^{III} (**2**), Dy^{III} (**3**), Ho^{III} (**4**), Er^{III} (**5**), Sm^{III} (**6**), L = 2-(thiophen-2-ylselanyl)acetic acid, phen = 1,10-phenanthroline) have been synthesized and characterized by powder X-ray diffraction and single-crystal X-ray diffraction analysis. Single crystal X-ray diffraction analysis showed that complexes **1**–**6** are isostructural and crystallize in the triclinic space group *P-1*. The luminescent properties and lifetimes of complexes **1**–**3** have been studied, which show the characteristic emissions of Eu^{III} ($^5D_0 \rightarrow {}^7F_{0\text{-}4}$), Tb^{III} ($^5D_4 \rightarrow {}^7F_{6\text{-}3}$) and Dy^{III} ($^4F_{9/2} \rightarrow {}^6H_{15/2,\ 13/2,\ 11/2,\ 9/2}$), and the corresponding luminescent lifetimes are 1.24 ms, 6.25 μs and 4.26 μs, respectively. The magnetic properties of the complexes **3** and **4** were also measured and exhibited weak anti-ferromagnetic interactions between Ln^{III} centers. Moreover, the complex **3** showed the properties of the potential single-molecule magnets with the energy barrier (*U/kB*) 47.50 K and the τ_0 9.73×10^{-8} s. In view of this, the Dy^{III} complex **3** displayed the behavior of the luminescent single-molecule magnets.

Keywords Lanthanide(III) coordination complexes · 2-(Thiophen-2-ylselanyl)acetic acid · Crystal structures · Magnetic properties · Photoluminescence properties

Introduction

In the past few decades, the lanthanide complexes have attracted worldwide interests due to their potential applications in the fields of sorption, catalysis, magnetism and photochemistry [1–3]. Since the milestone discovery of a terbium(III) bis(phthalocyaninato) complex displaying the phenomenon of single-molecule magnets (SMMs), which are molecular complexes exhibiting slow relaxation of the magnetization and magnetic hysteresis at low temperature, the designs and syntheses of lanthanide-based SMMs have experienced impressive development, and a large number of lanthanide-based SMMs have been reported, and some of them exhibited slow relaxation of the magnetization with high anisotropy barrier [4–7]. In the last decade, the rational designs of the multifunctional SMMs with other properties, in which the targeted compounds may exhibit different physical features when subjected to various external stimuli, have attracted the attention of many researchers [8–10]. Most lanthanide ions possess strong unquenched orbital angular momentum and large spin orbit coupling of the 4f electrons, they not only may contribute to the acquisition of single-molecule magnets but also contribute to the improvement of luminescence performance, so that lanthanide ions are a great choice for constructing the multifunctional SMMs [11–14]. The luminescent single-molecule magnets are a type of dual functional materials with magnetic and luminescent properties. The incorporation of two properties into one molecular entity is an effective way to obtain dual functional molecule-based materials [15–18].

The designs and synthesis of the luminescent SMMs requires consideration of many factors, such as metal ions and ligands. Lanthanide(III) ions, especially the Dy(III)

✉ Ru-Fen Zhang
zhangrufen@lcu.edu.cn

✉ Chun-Lin Ma
macl856@163.com

[1] Institution of Functional Organic Molecules and Materials, School of Chemistry and Chemical Engineering, Liaocheng University, Liaocheng 252059, China

[2] Experimental Middle School, Liaocheng 252059, China

ion, have not only a large spin ground state but also magnetic anisotropy, which can meet the two prerequisites for the appearance of the luminescent SMMs [19–23]. On the other hand choosing a suitable ligand can effectively produce an ''antenna effect'' to promote the regulation of its luminescent properties [24, 25]. Among various types of ligands, 2-thiophene carboxylate acid substituents containing unsaturated bonds and isolated electrons functional groups can transfer efficiently the energy of the π, π* excited state to lanthanide ions to increase their luminescence properties [26–30]. In addition, it is noteworthy that the 1,10-phenanthroline possessing multiple functional groups as chelating ligand can not only helps to stability of constructed complexes but also improve the fluorescence emissions [31, 32].

Given the aforementioned consideration, we chose 2-(thiophen-2-ylselanyl)acetic acid as the main ligand and 1,10-phenanthroline as the auxiliary ligand to synthesize six isostructural lanthanide complexes $[Ln_2(L)_6(phen)_2]$ (Ln = Eu^{III} (**1**), Tb^{III} (**2**), Dy^{III} (**3**), Ho^{III} (**4**), Er^{III} (**5**), Sm^{III} (**6**) L = 2-(thiophen-2-ylselanyl)acetic acid, phen = 1,10-phenanthroline). The structures of complexes **1**–**6** display dinuclear structures. The photoluminescence properties of complex **1**–**3** and the magnetic properties of complexes **3**–**4** have been investigated in the solid state. Furthermore, the Dy^{III} complex **3** displayed the phenomenon of the potential multifunctional SMMs with fluorescent properties.

Experimental Section

Materials and Physical Measurements

Lanthanide(III) chloride hexahydrate and 1,10-phenanthroline were commercially available and were all used without further purification. 2-(thiophen-2-ylselanyl)acetic acid was prepared by the method reported in the literatures [33, 34]. The contents of C, H and N were depicted in Vario-EL II elemental analyzer. IR spectra were recorded using the conventional KBr pellets technique by a Nicolet-5700 spectrometer (4000–400 cm^{-1}). The powder X-ray diffraction (PXRD) data of the samples were collected on a Rigaku Dmax 2000 X-ray diffractometer with graphite mono chromatized Cu Kα radiation (λ = 0.1542 nm) and 2θ ranging from 5° to 50°. The fluorescence spectra were collected on Edinburgh FLS 1000 fluorescence spectrometer. Magnetic properties were measured using a Quantum Design SQUID VSM magnetometer on polycrystalline samples. All magnetic data were corrected for the diamagnetism of the sample holder and constituent atoms according to Pascal's constants.

Syntheses of Complexes 1–6

Six dinuclear lanthanide(III) complexes were prepared with a molar ratio of 3:1:1. The syntheses methods of complexes **1**–**6** are similar, so complex **1** is taken as an example to describe the synthesis steps (Fig. 1).

A mixture of 2-(thiophen-2-ylselanyl)acetic acid (0.30 mmol), 1,10-phenanthroline (0.10 mmol) were dissolved in methanol, adjusting the pH of the solution to 5.8–6.2 with a KOH solution (0.2 mol/L). Then, the resulting solution was added dropwise into the turbid aqueous solution of $EuCl_3{\cdot}6H_2O$ (0.10 mmol) under stirring. After stirring at room temperature for 4 h, the filtered solution was left to stand for 10 days, and finally the block single crystals suitable for X-ray analysis were obtained.

$[Eu_2[(C_4H_3S)SeCH_2COO]_6(phen)_2]$ (**1**): Yield: 49.37%. Elemental analysis (%), calculated for $C_{60}H_{46}Eu_2N_4O_{12}S_6Se_6$: C, 36.34, H, 2.35, N, 2.79. Found: C, 36.52, H, 2.51,

Fig. 1 The syntheses of complexes **1**–**6**

Table 1 Crystallographic data and structure refinement parameters for complexes **1–6**

Complex	**1**	**2**	**3**	**4**	**5**	**6**
Empirical formula	$C_{60}H_{46}Eu_2N_4O_{12}S_6Se_6$	$C_{60}H_{46}Tb_2N_4O_{12}S_6Se_6$	$C_{60}H_{46}Dy_2N_4O_{12}S_6Se_6$	$C_{60}H_{46}Ho_2N_4O_{12}S_6Se_6$	$C_{60}H_{46}Er_2N_4O_{12}S_6Se_6$	$C_{60}H_{46}Sm_2N_4O_{12}S_6Se_6$
M	1985.05	1998.97	2006.13	2010.99	2015.65	1981.83
Crystal system	Triclinic	Triclinic	Triclinic	Triclinic	Triclinic	Triclinic
Space group	*P*-1	*P*-1	*P*-1	*P*-1	*P*-1	*P*-1
a [Å]	10.0600(9)	9.8482(9)	10.0884(9)	10.0576(9)	10.1230(9)	10.0388(9)
b [Å]	12.9690(11)	12.7279(12)	13.0297(11)	12.9641(11)	13.0051(11)	13.0576(12)
c [Å]	13.9500(12)	13.6467(13)	13.9528(12)	13.9100(12)	13.9969(11)	13.9125(11)
α [°]	108.207(4)	108.347(3)	108.398(3)	108.374(3)	108.263(3)	108.285(3)
β [°]	99.059(2)	99.244(2)	99.257(2)	99.183(2)	99.140(2)	99.390(2)
γ [°]	93.0880(10)	92.8350(10)	92.7360(10)	92.7060(10)	92.6610(10)	92.9920(10)
V [Å^3]	1697.0(3)	1593.4(3)	1708.1(3)	1689.9(3)	1718.5(3)	1698.0(3)
Z	1	1	1	1	1	1
Dcalc (Mg/m^3)	1.942	2.083	1.950	1.976	1.948	1.938
μ (mm^{-1})	5.294	5.889	5.611	5.801	5.844	5.173
F(000)	956	960	962	964	966	954
Crystal size(mm)	0.21 × 0.18 × 0.06	0.12 × 0.11 × 0.04	0.21 × 0.11 × 0.05	0.19 × 0.10 × 0.05	0.18 × 0.17 × 0.11	0.18 × 0.11 × 0.05
Reflections collected	8654	8310	8719	8634	8739	8606
Unique reflections	5874	5564	5918	5864	5952	5903
Goodness-of-fit on F^2	1.002	0.928	1.010	0.950	0.921	0.956
Final R indices [$I > 2\sigma(I)$]	$R_1{}^a = 0.0524$	$R_1{}^a = 0.0919$	$R_1{}^a = 0.0643$	$R_1{}^a = 0.0759$	$R_1{}^a = 0.0611$	$R_1{}^a = 0.0621$
	$wR_2{}^b = 0.1355$	$wR_2{}^b = 0.2233$	$wR_2{}^b = 0.1711$	$wR_2{}^b = 0.1748$	$wR_2{}^b = 0.1404$	$wR_2{}^b = 0.1583$
R indices (all data)	$R_1 = 0.0687$	$R_1 = 0.1262$	$R_1 = 0.0845$	$R_1 = 0.1318$	$R_1 = 0.0967$	$R_1 = 0.0941$
	$wR_2 = 0.1427$	$wR_2 = 0.2455$	$wR_2 = 0.1833$	$wR_2 = 0.1958$	$wR_2 = 0.1531$	$wR_2 = 0.1743$

[a] $R_1 = \sum||F_o|-|F_c||/\sum|F_o|$; [b] $wR_2 = \{\sum[w(F_o{}^2-F_c{}^2)^2]/\sum[w(F_o{}^2)^2]\}^{1/2}$

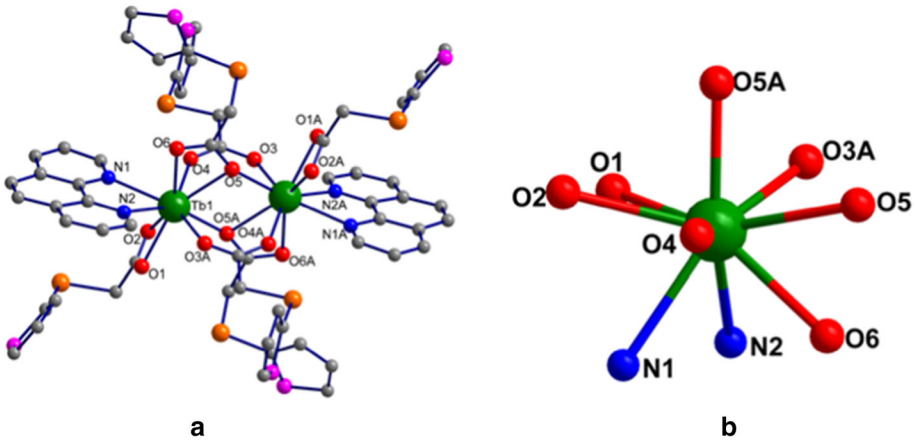

Fig. 2 **a** Molecular structure of complex **2** (H atoms were omitted for clarity); **b** View of the environment of the nine-coordinated Tb^{III} ion with a tricapped triangular prism Symmetry codes: A, − *x*, 1− *y*, 2− *z*

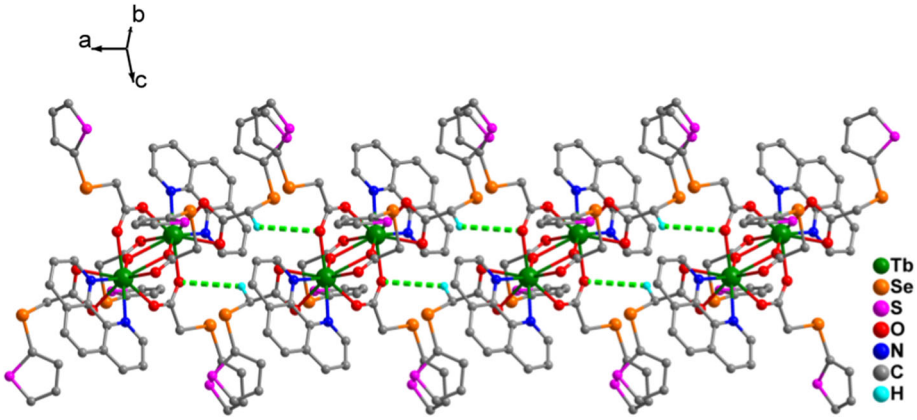

Fig. 3 The infinite 1D chain structure of complex **2**. (H atoms were omitted for clarity)

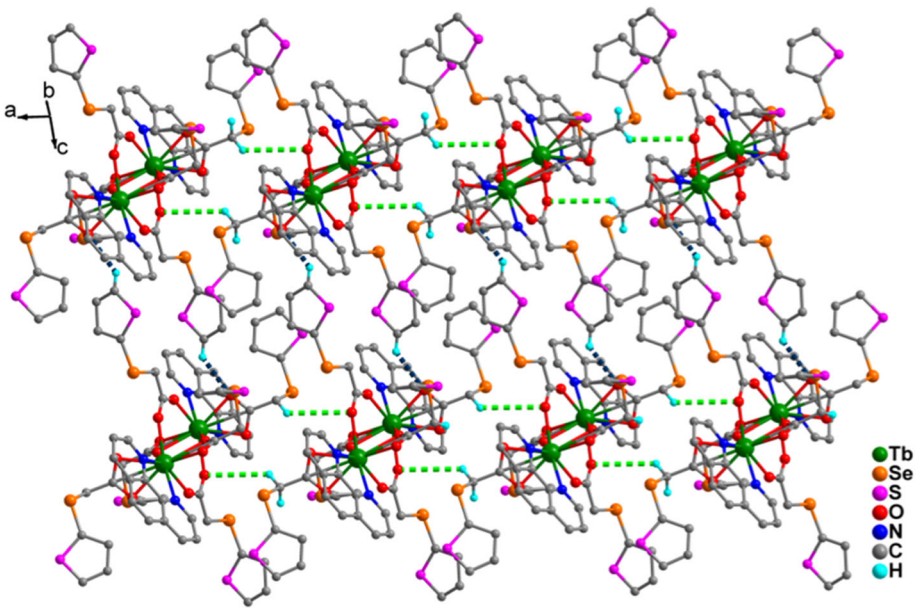

Fig. 4 The 2D layer supramolecular structure of the complex **2**. (H atoms were omitted for clarity)

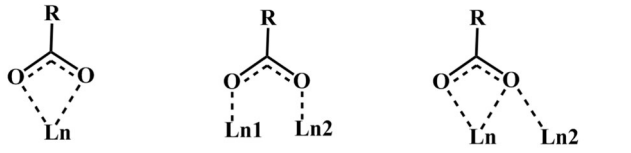

Fig. 5 The coordination modes of the ligands in complexes **1–6**

N, 2.92. IR data (KBr, cm^{-1}): 3426(w), 3081(w), 1602(s), 1589(m), 1545(m), 1516(s), 1436(s), 1386(s), 1348(w), 1215(w), 1188(w), 1140(w), 1102(w), 1047(w), 961(w), 864(s), 844(s), 773(w), 729(m), 697(m), 687(s), 670(w), 417(w).

$[Tb_2[(C_4H_3S)SeCH_2COO]_6(phen)_2]$ (**2**): Yield: 48.95%. Elemental analysis (%), calculated for $C_{60}H_{46}Tb_2N_4O_{12}S_6Se_6$: C, 36.05, H, 2.32, N, 2.80. Found: C, 36.22, H, 2.46, N, 2.99. IR data (KBr, cm^{-1}): 3424(w), 3082(w), 1603(s), 1590(m), 1547(m), 1517(s), 1439(s), 1387(s), 1348(w), 1215(w), 1189(w), 1139(w), 1102(w), 1047(w), 963(w), 864(m), 844(s), 773(w), 729(m), 698(m), 688(s), 418(w).

$[Dy_2[(C_4H_3S)SeCH_2COO]_6(phen)_2]$ (**3**): Yield: 54.37%. Elemental analysis (%), calculated for $C_{60}H_{46}Dy_2N_4O_{12}S_6Se_6$: C, 35.92, H, 2.31, N, 2.79. Found: C, 35.78, H, 2.19, N, 2.63. IR data (KBr, cm^{-1}): 3422(w), 3083(w), 1603(s), 1590(m), 1548(m), 1517(s), 1440(s), 1387(s), 1348(w), 1218(w), 1189(w), 1139(w), 1102(w), 1047(w), 964(w), 864(s), 843(s), 773(w), 729(m), 698(m), 688(s), 671(w), 418(w).

$[Ho_2[(C_4H_3S)SeCH_2COO]_6(phen)_2]$ (**4**): Yield: 51.67%. Elemental analysis (%), calculated for $C_{60}H_{46}Ho_2N_4O_{12}S_6Se_6$: C, 35.83, H, 2.31, N, 2.79. Found: C, 36.07, H, 2.44, N, 2.95. IR data (KBr, cm^{-1}): 3416(w), 3084(w), 1604(s), 1590(m), 1550(m), 1517(s), 1441(s), 1388(s), 1348(w), 1215(w), 1189(w), 1139(w), 1103(w), 1047(w), 964(w), 864(s), 843(s), 773(w), 729(m), 698(m), 689(s), 672(w), 418(w).

$[Er_2[(C_4H_3S)SeCH_2COO]_6(phen)_2]$ (**5**): Yield: 32.46%. Elemental analysis (%), calculated for $C_{60}H_{46}Er_2N_4O_{12}S_6Se_6$: C 35.75, H 2.30, N 2.78. Found: C, 35.55, H, 2.15, N, 2.60. IR data (KBr, cm^{-1}): 3439(w), 3085(w), 1604(s), 1590(m), 1551(m), 1517(s), 1443(s), 1388(s), 1347(w), 1215(w), 1190(w), 1139(w), 1103(w), 1048(w), 965(w), 864(s), 843(s), 773(w), 729(m), 698(m), 689(s), 673(w), 418(w).

$[Sm_2[(C_4H_3S)SeCH_2COO]_6(phen)_2]$ (**6**): Yield: 48.95%. Elemental analysis (%), calculated for $C_{60}H_{46}Sm_2N_4O_{12}S_6$: C, 36.36, H, 2.34, N, 2.83. Found: C, 36.21, H, 2.22, N, 2.69. IR data (KBr, cm^{-1}): 3422(w), 3082(w), 1598(s), 1588(m), 1542(m), 1516(s), 1430(s), 1385(s), 1215(w), 1187(w), 1139(w), 1101(w), 960(w), 863(s), 843(s), 773(w), 729(m), 696(m), 685(s), 668(w), 417(w).

X-ray Crystallography

Single-crystal X-ray diffraction data for the complexes **1–6** were collected on a Bruker SMART-1000 CCD diffractometer with graphite-monochromated Mo K_α radiation (λ = 0.71073 Å) radiation at room temperature. The data were integrated and corrected for Lorentz and polarization effects using SAINT [35]. Absorption corrections were applied with SADABS [36]. The structures were solved by direct methods and refined by the full-matrix least-squares method on F^2 using the SHELXTL crystallographic software package [37]. During the final cycles, the atoms were refined anisotropically. Hydrogen atoms were placed in calculated positions and refined as riding atoms. Some constraints (SIMU, DELU and ISOR instructions in SHELXL2014) on the anisotropic displacement parameters were applied in the refinement procedures to restrain the

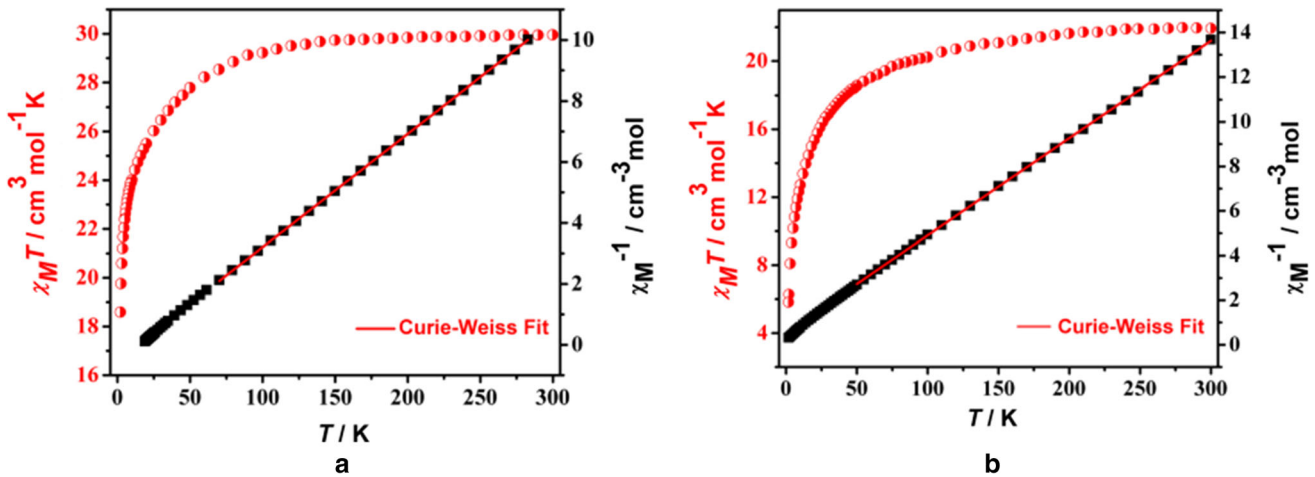

Fig. 6 **a** Temperature dependence of the $\chi_M T$ *vs.* T and $\chi_M{}^{-1}$ *vs.* T curve for complex **3**; **b** Temperature dependence of the χ_MT *vs.* T and $\chi_M{}^{-1}$ *vs.* T curve for complex **4**. The red line represents Curie–Weiss fit

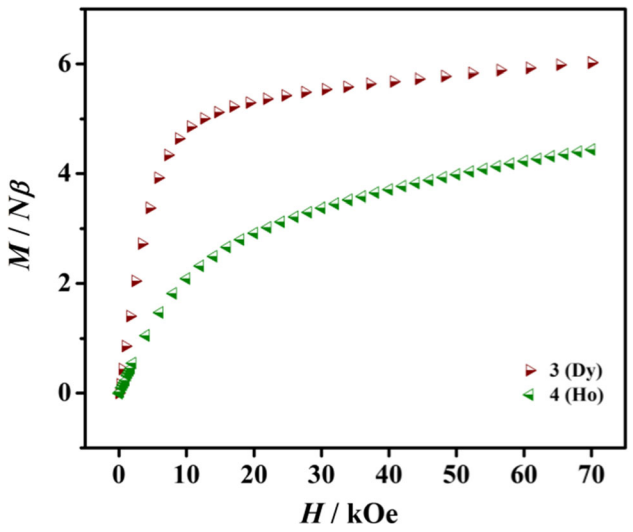

Fig. 7 Field-dependent magnetizations for complexes **3** and **4**

thermal ellipsoid [37, 38]. Crystallographic data and structural refinement details of complexes **1–6** are summarized in Table 1. Selected bond lengths and bond angles of complex **1–6** are listed in Tables S2 to S7.

Results and Discussion

Crystal Structure Descriptions

X-ray crystallographic study reveals that complexes **1–6** are isostructural except for the distinction of the lanthanide ion. Each of them is a dinuclear structure and crystallizes in the Triclinic space group P-1 with Z = 1, thus complex **2** is selected as a representative of the six complexes to discuss their structures in detail. As is shown in Fig. 2, complex **2** is composed of two Tb^{III} ions, six deprotonated 2-(thiophen-2-ylselanyl)acetic acid ligand, one 1,10-phenanthroline molecule. Every Tb^{III} centre is surrounded by nine atoms, exhibiting a tricapped triangular prism geometry with seven oxygen atoms and two nitrogen atoms, two oxygen atoms (O1, O2) from one chelating deprotonated 2-(thiophen-2-ylselanyl)acetic acid ligand, three oxygen atoms (O3A, O4, μ_2-O5A) from three bridging deprotonated ligands, two oxygen atoms (μ_2-O5, O6) from one bridging deprotonated ligand, and two nitrogen atoms (N1, N2) from one chelating 1,10-phenanthroline molecule. Using the program SHAPE 2.1 [39], the continuous shape measures (CShMs) of the Tb^{III} centers relative to the ideal C_s symmetry is calculated to be 5.631. The Tb-O bond distances range from 2.299(5) to 2.481(5) Å, and the Tb-N bond distances range from 2.496(7) to 2.625(6) Å, which are within the bond distances of Tb-O and Tb-N of the previous terbium complexes [40, 41]. The intramolecular $Tb^{III}\cdots Tb^{III}$ distances of 3.828 Å, which are within the of $Tb^{III}\cdots Tb^{III}$ distances reported for lanthanide clusters [42].

The adjacent dinuclear complexes extend along a axis direction to form a one-dimensional (1D) chain through the C–H···O (C5–H5···O4, 2.287 Å) intermolecular hydrogen bond interaction (Fig. 3). Furthermore, such 1D chains assemble into 2D layers supramolecular architecture via the C–H···O (C7–H7···O1, 2.439 Å) hydrogen bonding interactions in the a c plane (Fig. 4).

In complex **2**, the deprotonated 2-(thiophen-2-ylselanyl)acetic acid adopt multiple coordination modes with k(O,O′) chelating mode, and μ-1 k(O);2 k(O′) or μ-1 k(O,O′);2 k(O′) bridge modes to connect Tb atoms into dinuclear coordination complex (Fig. 5) [43].

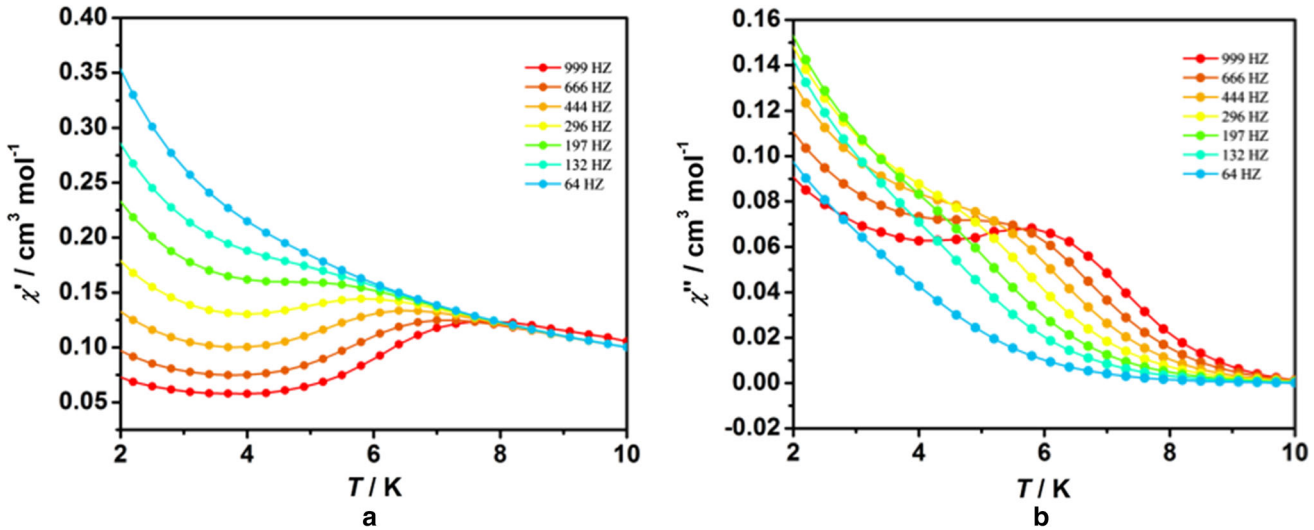

Fig. 8 Temperature dependence of the χ' and χ'' ac susceptibilities under zero dc field for complex **3**

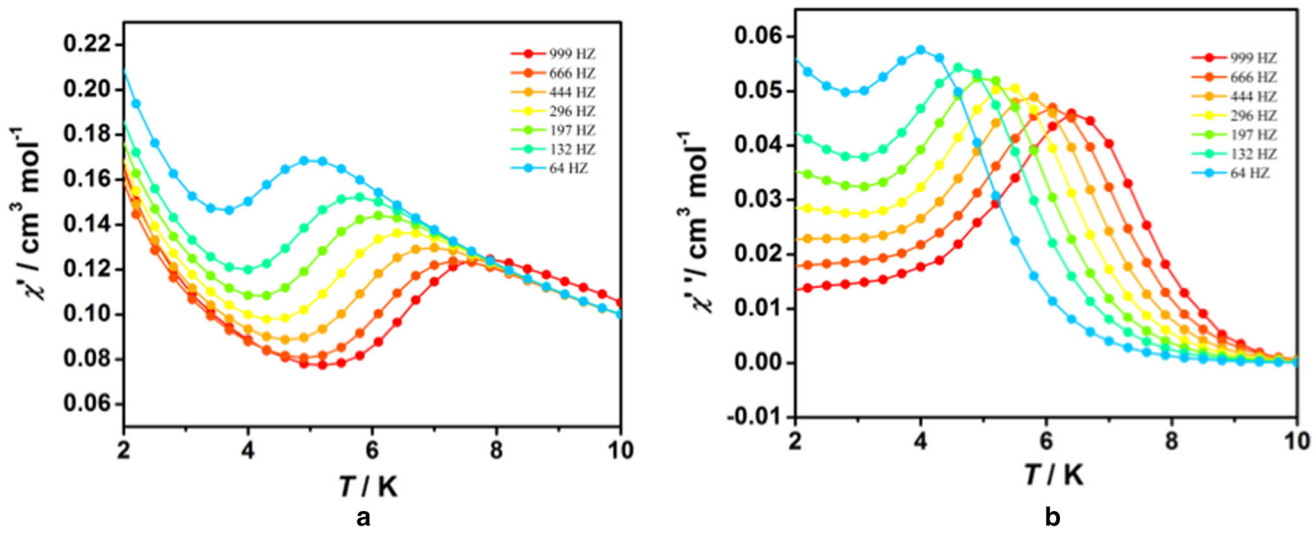

Fig. 9 Temperature dependence of the χ' and χ'' ac susceptibilities under 1 kOe dc field for complex **3**

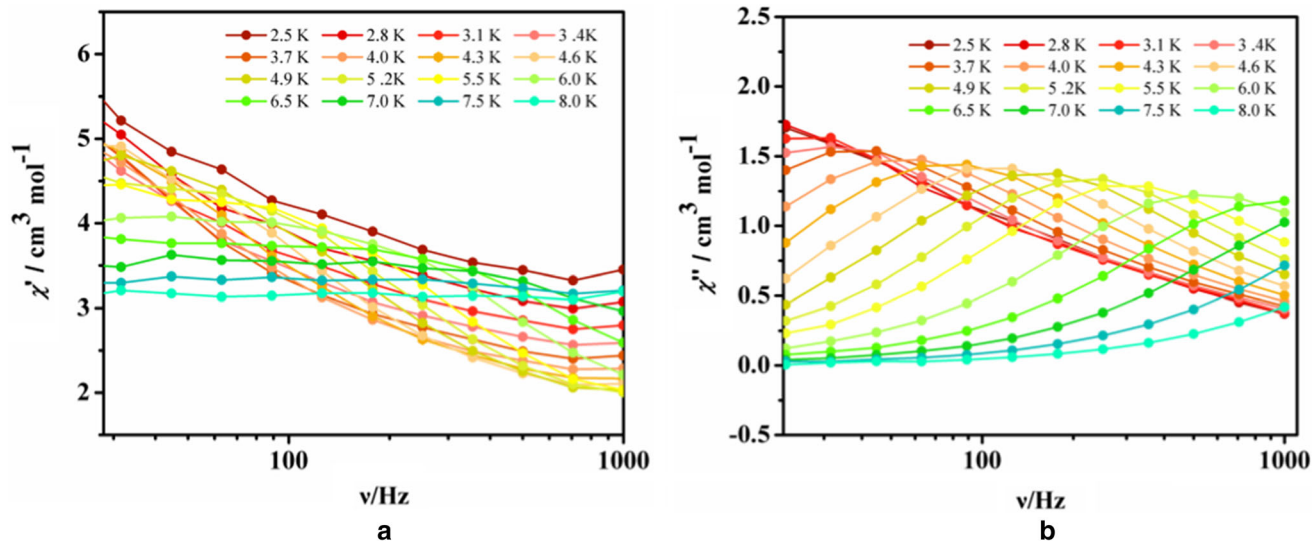

Fig. 10 Frequency dependence of the χ' and χ'' ac susceptibilities under 1 kOe dc field for complex **3**

Powder X-ray Diffraction and Thermogravimetric Analyses of Complexes 1–6

In order to evaluate the phase purity of complexes **1**–**6**, powder X-ray diffraction patterns experiments have been performed at the room temperature. The PXRD patterns of complexes **1**–**6** are shown in Figs. S7 to S12, respectively. Their high purity solid state phases were confirmed by the good matching the measured and simulated PXRD patterns.

The thermogravimetric analyses (TGA) of complexes **1**–**6** are measured in the temperature range from 25 to 800 °C under nitrogen atmosphere with a heating rate of 20 K min^{-1} (Fig. S13). The weight loss behaviours of complexes **1**–**6** are similar and there is only one step of weight loss in the temperature region of 250–310 °C. The TGA results of complexes **1**–**6** indicate good thermal stability.

Magnetic Properties

Static Magnetic Properties

The variable-temperature magnetic susceptibility measurements for **3** and **4** were carried out over the temperature range of 2 to 300 K in alternating current field of 1 kOe. The plots of $\chi_M T$ and ${\chi_M}^{-1}$ versus T are shown in Fig. 6a for **3** and Fig. 6b for **4**. The experimental $\chi_M T$ values at 300 K are 29.96 cm^3 mol^{-1} K for **3** and 21.94 cm^3 mol^{-1} K for **4**, respectively, which are approached to the

expected values of Ln^{III} ions (Dy^{III}: 28.34 cm^3 mol^{-1} K, S = 5/2, L = 5, g = 4/3; Ho^{III}: 28.14 cm^3 mol^{-1} K, S = 2, L = 6, g = 5/4). With decreasing temperature, the χ_MT values exhibit very slow decrease down to 50 K and then sharply decrease in the lower temperature regions, at 2 K reach a minimum of 9.30 cm^3 mol^{-1} K for **3** and 2.91 cm^3 mol^{-1} K for **4**. This behavior should be ascribed to depopulation of the excited Stark sublevels from the crystal-field splitting of Ln^{III} ions and/or antiferromagnetic interactions. This similar features was found in the reported Ln^{III} complexes $[Dy_2(HMBA)_2(MBA)_2(DMF)_2(H_2O)_2]\bullet 6H_2O$ and $\{[Ho_2(Hpimda)_2(\mu_4\text{-}C_2O_4)]\ 2H_2O\ 4H_2O\}_n$ [44, 45]. By analyzing of χ_M^{-1} versus T, the magnetic susceptibility obeys the Curie–Weiss law, $\chi_M = C/(T\text{-}\theta)$, between 50 and 300 K with Curie constant C are 30.39 cm^3 mol^{-1} K for **3** and 22.93 cm^3 mol^{-1} K for **4**, the Weiss constant θ are − 3.83 K for **3** and − 12.80 K for **4**, and then the negative Weiss constant values further exhibits weak antiferromagnetic indicated anti-ferromagnetic interactions between Ln^{III} ions [46].

The field dependencies of the magnetization were performed in the magnetic field range 0–70 kOe at 2 K for **3** and **4**. As shown in Fig. 7, the magnetization values first increase rapidly and then increase slowly with increased field and reach the values of 6.0 $N\beta$ for **3** and 4.5 $N\beta$ for **4** at 70 kOe. The observed saturation values for **3** and **4** are lower than the calculated values, which may be ascribed to the crystal field effects, low-lying excited states and/or significant magnetic anisotropy. The similar phenomenon was found in the other reported Dy^{III} and Ho^{III} clusters complexes [47, 48].

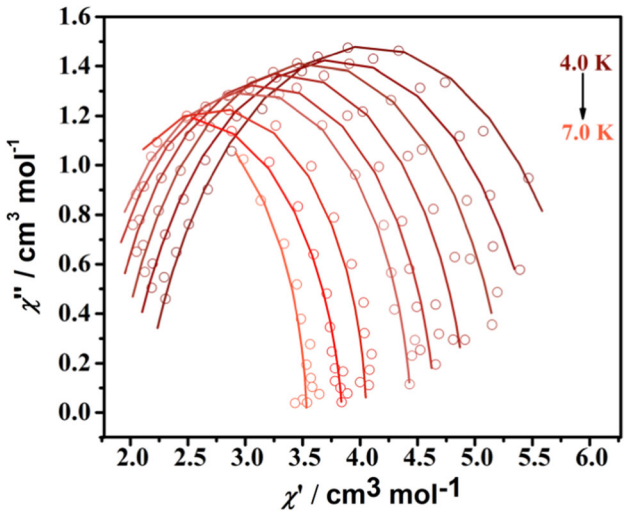

Fig. 11 Cole–Cole curves of complex **3** Solid lines represent the best fit with Debye model

Dynamic Magnetic Properties

In order to explore the potential slow magnetic relaxation of Dy^{III} complex **3**, which may originate from SMMs behavior, alternating current (ac) magnetic susceptibility measurements were performed at various temperatures and frequencies. As shown in Fig. 8, under zero dc fields, both in-phase (χ') and out-of-phase (χ'') signals clearly were observed in the temperature range of 2.0–10 K, but no peaks maxima were observed even at a low temperature and high frequency. The upturning and tailing of the curve in the low temperature area indicates that there is a significant QTM effect in the system. In order to study the relaxation behavior more clearly, an external magnetic field of 1000 Oe was applied. The QTM in the system was effectively suppressed. As shown in Fig. 9, the out-of-phase (χ'') signals exhibit well-shaped peaks, which shift

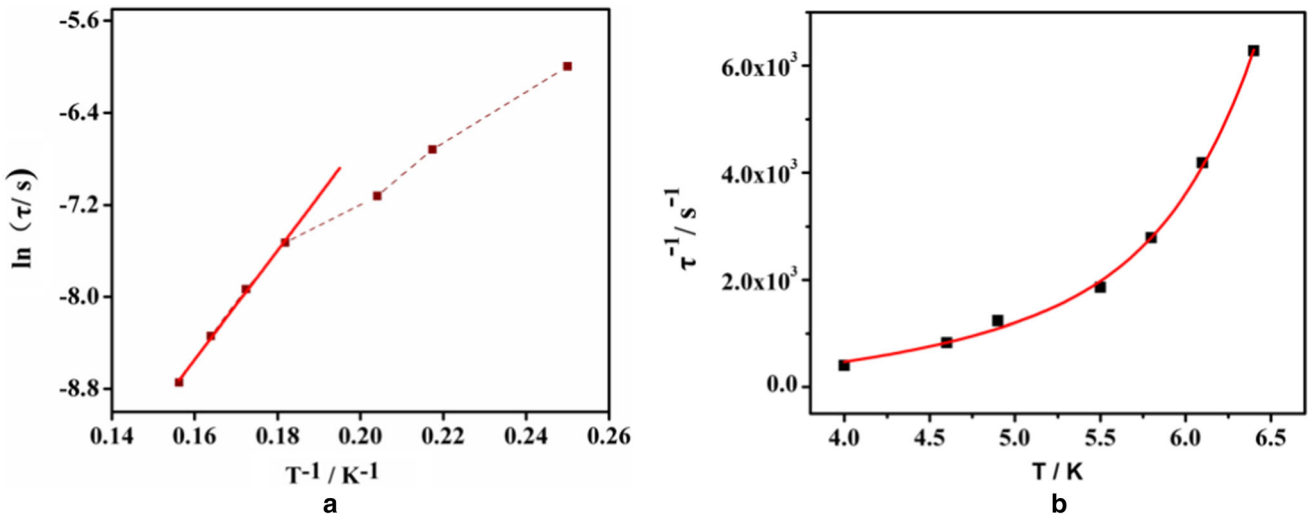

Fig. 12 **a** lnτ *vs.* T^{-1} plot for complex **3**, the solid line represents the best fits using the Arrhenius law. **b** τ^{-1} *vs.* T plot for complex **3**, the red curve represents the best fits using the Orbach plus Raman law

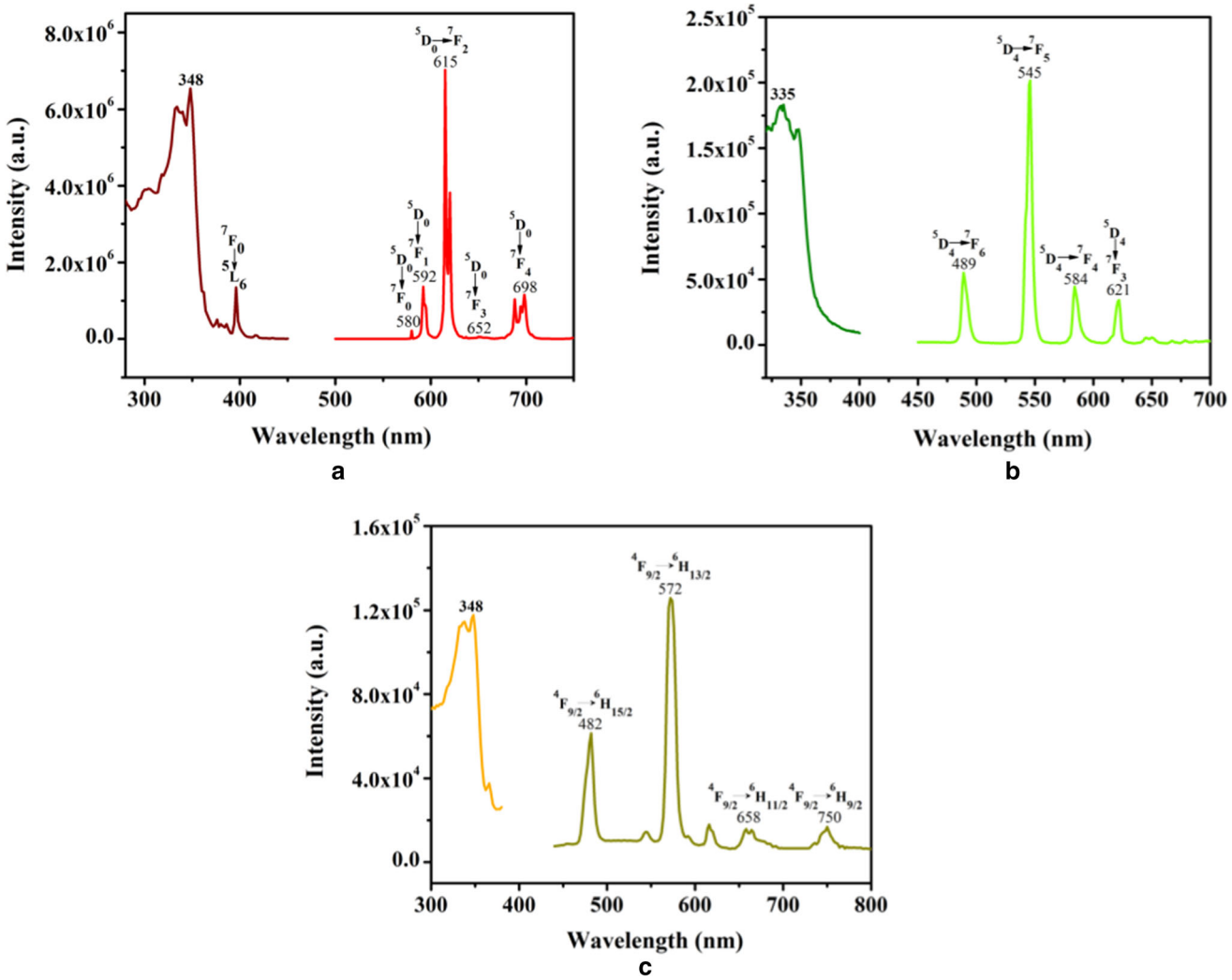

Fig. 13 The solid-state excitation and emission spectra of complexes **1** (**a**), **2** (**b**), **3** (**c**) at room temperature

gradually to lower frequencies with the decrease of temperature. In other words, as shown in Fig. 10, the imaginary part (χ'') can clearly display strong frequency dependence in the frequency range of 2.5–999 Hz, suggesting characteristic magnet relaxation of the SMMs [49, 50]. Furthermore, the relaxation times (τ) are obtained by applying the generalized Debye law in a range from 4.0 to 7.0 K (Fig. 11), giving the parameters α of 3.607×10^{-2}–1.795×10^{-1} listed in Table S9. The similar parameter values were observed for other Dy^{III} SMMs [51, 52]. At high temperature range, satisfactory results can be achieved by analyzing $\ln(\tau)$ versus T^{-1} using the Arrhenius law $\tau = \tau_0 \exp(U/k_BT)$. As shown in Fig. 12a, the resulting best-fit parameters are an energy barrier U/k_B of 47.5 K and τ_0 of 9.73×10^{-8} s, and U/k_B parameters agrees well with some examples of reported lanthanide clusters (Table S10) [53–56]. Nevertheless, τ becomes weakly dependent on T with decreasing temperature, which is possibly due to the mixture of the Orbach process and other relaxation processes. Moreover, the suitable fit was obtained by considering contributions from a Raman and an Orbach processes, $\tau^{-1} = CT^n + \tau_0^{-1} \exp(-U/k_BT)$, the resulting best-fit parameters are an energy barrier $U/k_B = 53.28$ K, $C = 0.29\ s^{-1}\ K^{-4.86}$, $n = 4.86$, $\tau_0 = 6.48 \times 10^{-8}$ s. The n value of 4.86 is reasonable value ($1 < n < 6$), and the τ_0 value falls within the normal range ($\tau_0 = 10^{-6}$–10^{-11}), which is consistent with the properties of the reported single-molecule magnets [57–59]. Based on the above research, the Dy^{III} complex **3** exhibited the behavior of single molecule magnets.

Photoluminescence Properties

The trivalent lanthanide ions are wide researched for their photoluminescence properties in the visible and near-infrared regions, which endows Ln^{3+} luminescent materials

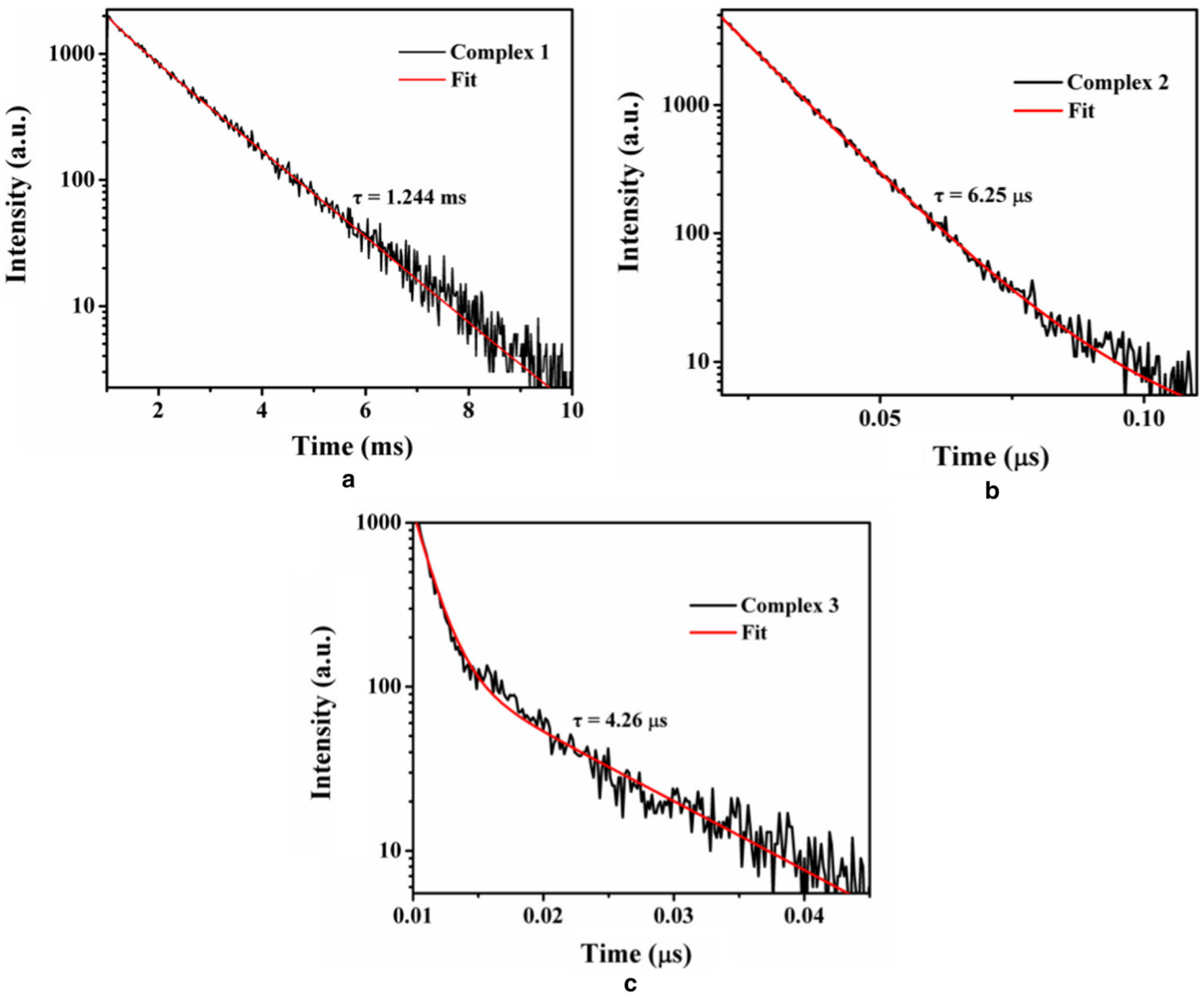

Fig. 14 The luminescence decay curve of complexes **1** (**a**), **2** (**b**), **3** (**c**) with the double exponential behavior

with wide applications in photonic devices. Based on this, the solid-state luminescent properties of the complexes **1**–**3** have been investigated at room temperature. Their excitation and emission spectra and lifetime decay behaviors are shown in Figs. 13 and 14, corresponding colour coordinates are shown in Fig. S14.

The excitation spectra of complexes **1**–**3** all show broad band, which are attributed to the π–π* transition of the ligands. Excitation of complex **1** (Fig. 13a), Eu^{III} displays weak characteristic f-f transitions at 396 nm, which can be reasonably assigned to the $^7F_0 \rightarrow {}^5L_6$ transitions of Eu^{III}. The f–f transitions are weaker than the ligand-bands, which suggest the better sensitization of Eu^{III} ions luminescence through ligand excitation. Such the properties of complex **1** has been also found in other Eu-selenoacetic complex, $[Eu_2L_6(phen)_2]$ (L = 4-fluorophenylselenoacetate) [60]. Eu^{III} complex displays five characteristic sharp emission bands at 580, 592, 615, 652, and 698 nm under the excitation of 348 nm (Fig. 13a), which can be assigned to the $^5D_0 \rightarrow {}^7F_{0-4}$ transitions, respectively. The intensity of the $^5D_0 \rightarrow {}^7F_2$ transition, which is extremely sensitive to site symmetry, is stronger than the $^5D_0 \rightarrow {}^7F_1$ transition. Therefore, the Eu^{III} ion in complex **1** should occupy sites with a low symmetry and no inversion center should be present for these sites. The similar result is also found in $\{[Eu(L_1)(DMF)(H_2O)]\cdot DMF\}_n$ (5-(2′-carboxylphenoxy)isophthalic acid) [61]. As shown in Fig. S14a, the CIE chromaticity coordinate values of complex **1** are (0.6629, 0.3367) and ‘‘red’’ emission is emitted. The emission spectra of complex **2** (Fig. 13b), Tb^{III} complex displays four characteristic sharp emission bands at 489, 545, 584, 621 nm under the excitation of 335 nm, which can be assigned to the $^5D_4 \rightarrow {}^7F_{6-3}$ transitions, respectively. The most intense peak at 545 nm represents the

$^5D_4 \rightarrow {}^7F_5$ transition, which shows the green light emission for Tb^{III} ions with a CIE chromaticity coordinate of (0.3425, 0.5639) (Fig. S14b). The emission spectra of complex **3** (Fig. 13c), Dy^{III} complex displays four characteristic sharp emission bands at 482, 572, 658, 750 nm under the excitation of 348 nm, which can be assigned to the $^4F_{9/2} \rightarrow {}^6H_J$ (15/2, 13/2, 11/2, 9/2) transitions, respectively. Notably, the Dy^{III} complex emits a yellow light with a CIE coordinate of (0.3873, 0.4317) (Fig. S14c). In addition, it is found that there is no apparent residual ligand-based luminescence emission in complexes **1–3**, indicating that Eu^{III} and Tb^{III} and Dy^{III} centres can be efficiently sensitized by the ligands [62, 63].

The luminescence decay curve can be well fitted to the double-exponential function as $I = A_1 \exp(-t/\tau_1) + A_2 \exp(-t/\tau_2)$ (where τ_1 and τ_2 are the fast and slow components of the luminescence lifetimes, A_1 and A_2 are the pre-exponential factors). And then, based on $\tau = (A_1\tau_1^2 + A_2\tau_2^2)/(A_1\tau_1 + A_2\tau_2)$ and τ is the luminescent lifetime [64, 65], yielding the average lifetimes values of around 1.24 ms for **1**, 6.25 μs for **2**, 4.26 μs for **3,** which are moderate compared to previous reports [66–68]. Furthermore, photoluminescence quantum yields of complexes **1** and **3** are also determined by the integration sphere method, which are 23.10% and 1.30%, respectively. The value for complex **2** is too small (< 1%) to be measured accurately. These preliminary results indicate that the energy transfer from the ligands to Ln^{III} ions is efficient [68–70].

Conclusions

In summary, new six lanthanide(III) complexes were successfully synthesized and characterized. The single X-ray crystallography study reveal that the lanthanide(III) ions adopt a nine-coordinated tricapped triangular prism geometry and adjacent molecules are connected by hydrogen bonding interactions to form infinite 1D chain structures and 2D layers. The solid-state luminescent spectra demonstrated that complexes **1–3** respectively exhibited strong characteristic emissions. Magnetic studies revealed that the anti-ferromagnetic interactions existed between the adjacent Ln^{3+} ions complexes **3** and **4**. Moreover, the complex **3** showed the phenomenon of the single-molecule magnets with the energy barrier (*U/kB*) 47.50 K and the τ_0 9.73×10^{-8} s. In view of this, the Dy^{III} complex **3** displayed the phenomenon of the luminescent SMMs, which offers valuable information for the designs and syntheses of the lanthanide-based multifunctional single-molecule magnets.

Supplementary Information The online version contains supplementary material available at https://doi.org/10.1007/s10876-022-02266-x.

Acknowledgements We thank the National Natural Science Foundation of China (Grant No. 21371087), Natural Science Foundation of Shandong Province (Grant Nos. ZR2018LB003, ZR2020MB019) for financial support.

References

1. A. Topor, D. Liu, C. Maxim, G. Novitchi, C. Train, Z. A. AlOthman, A. A. S. Al-Kahtani, L. Ungur, L. T. A. Ho, L. F. Chibotaru, and M. Andruh (2021). *J. Mater. Chem. C* **9**, 10912–10926.
2. C. Theppitak, F. Kielar, W. Dungkaew, M. Sukwattanasinitt, L. Kangkaew, S. Sahasithiwat, H. Zenno, S. Hayami, and K. Chainok (2021). *RSC Adv.* **11**, 24709–24721.
3. S. Dey and G. Rajaraman (2020). *Dalton Trans.* **49**, 14781–14785.
4. N. Ishikawa, M. Sugita, T. Ishikawa, S.-Y. Koshihara, and Y. Kaizu (2003). *J. Am. Chem. Soc.* **125**, 8694–8695.
5. F.-S. Guo, M. Day Benjamin, Y.-C. Chen, M.-L. Tong, A. Mansikkamäki, and A. Layfield Richard (2018). *Science* **362**, 1400–1403.
6. Z. Zhu, C. Zhao, T. Feng, X. Liu, X. Ying, X.-L. Li, Y.-Q. Zhang, and J. Tang (2021). *J. Am. Chem. Soc.* **143**, 10077–10082.
7. F. Liu, D. S. Krylov, L. Spree, S. M. Avdoshenko, N. A. Samoylova, M. Rosenkranz, A. Kostanyan, T. Greber, A. U. B. Wolter, B. Büchner, and A. A. Popov (2017). *Nat. Commun.* **8**, 16098.
8. J. Long, J. Rouquette, J.-M. Thibaud, R. A. S. Ferreira, L. D. Carlos, B. Donnadieu, V. Vieru, L. F. Chibotaru, L. Konczewicz, J. Haines, Y. Guari, and J. Larionova (2015). *Angew. Chem. Int. Ed.* **54**, 2236–2240.
9. J.-Y. Wang, Y. Shi, D.-L. Tao, G.-Y. Yin, and Q.-B. Bo (2020). *CrystEngComm* **22**, 4449–4467.
10. J. Long, R. Vallat, R. A. S. Ferreira, L. D. Carlos, F. A. Almeida Paz, Y. Guari, and J. Larionova (2012). *Chem. Commun.* **48**, 9974–9976.
11. M. Nie, L. Yang, C. Zhao, H. Meng, L. Feng, P. Jin, C. Wang, and T. Wang (2019). *Nanoscale* **11**, 18612–18618.
12. G. Cucinotta, M. Perfetti, J. Luzon, M. Etienne, P.-E. Car, A. Caneschi, G. Calvez, K. Bernot, and R. Sessoli (2012). *Angew. Chem. Int. Ed.* **51**, 1606–1610.
13. D. S. Krylov, F. Liu, S. M. Avdoshenko, L. Spree, B. Weise, A. Waske, A. U. B. Wolter, B. Büchner, and A. A. Popov (2017). *Chem. Commun.* **53**, 7901–7904.
14. R. Westerström, J. Dreiser, C. Piamonteze, M. Muntwiler, S. Weyeneth, H. Brune, S. Rusponi, F. Nolting, A. Popov, S. Yang, L. Dunsch, and T. Greber (2012). *J. Am. Chem. Soc.* **134**, 9840–9843.
15. Q.-Q. Su, K. Fan, X.-X. Jin, X.-D. Huang, S.-C. Cheng, L.-J. Luo, Y.-J. Li, J. Xiang, C.-C. Ko, L.-M. Zheng, and T.-C. Lau (2019). *Inorg. Chem. Front.* **6**, 1442–1452.
16. J.-H. Jia, Q.-W. Li, Y.-C. Chen, J.-L. Liu, and M.-L. Tong (2019). *Coord. Chem. Rev.* **378**, 365–381.
17. J. Long, Y. Guari, R. A. S. Ferreira, L. D. Carlos, and J. Larionova (2018). *Coord. Chem. Rev.* **363**, 57–70.
18. H.-F. Wang, J.-X. Tang, H.-H. Zou, and F.-P. Liang (2020). *J. Clust. Sci.* **31**, 1155–1161.
19. F. Pointillart, B. L. Guennic, S. Golhen, O. Cador, O. Maury, and L. Ouahab (2013). *Chem. Commun.* **49**, 615–617.

20. R. Sessoli and A. K. Powell (2009). *Coord. Chem. Rev.* **253**, 2328–2341.
21. S. Chorazy, M. Rams, K. Nakabayashi, B. Sieklucka, and S.-I. Ohkoshi (2016). *Chem. Eur. J.* **22**, 7371–7375.
22. J. Ruiz, A. J. Mota, A. Rodríguez-Diéguez, S. Titos, J. M. Herrera, E. Ruiz, E. Cremades, J. P. Costes, and E. Colacio (2012). *Chem. Commun.* **48**, 7916–7918.
23. S. Chorazy, J. Wang, and S.-I. Ohkoshi (2016). *Chem. Commun.* **52**, 10795–10798.
24. W.-Q. Zhang, R.-F. Zhang, Q.-F. Zhang, S.-L. Zhang, J. Ru, Q.-L. Li, and C.-L. Ma (2019). *Solid State Chem.* **270**, 360–365.
25. A. S. Kalyakina, V. V. Utochnikova, M. Zimmer, F. Dietrich, A. M. Kaczmarek, R. Van Deun, A. A. Vashchenko, A. S. Goloveshkin, M. Nieger, M. Gerhards, U. Schepers, and S. Bräse (2018). *Chem. Commun.* **54**, 5221–5224.
26. R. J. Batrice, A. K. Adcock, P. M. Cantos, J. A. Bertke, and K. E. Knope (2017). *Cryst. Growth Des.* **17**, 4603–4612.
27. K. E. Horner and P. B. Karadakov (2013). *J. Org. Chem.* **78**, 8037–8043.
28. F. Cagnin, M. R. Davolos, and E. E. Castellano (2014). *Polyhedron* **67**, 65–72.
29. C.-H. Zhan, F. Wang, Y. Kang, and J. Zhang (2012). *Inorg. Chem.* **51**, 523–530.
30. Y.-G. Sun, B. Jiang, T.-F. Cui, G. Xiong, P. F. Smet, F. Ding, E.-J. Gao, T.-Y. Lv, K. Van den Eeckhout, D. Poelman, and F. Verpoort (2011). *Dalton Trans.* **40**, 11581–11590.
31. C.-M. Liu, D.-Q. Zhang, and D.-B. Zhu (2016). *Chem. Commun.* **52**, 4804–4807.
32. J. Ye, Q. Wang, H. Gao, X. Lu, W. Gong, Y. Lin, and G. Ning (2012). *Inorg. Chim. Acta* **384**, 1–7.
33. W. H. H. Günther and M. N. Salzman (1972). *Ann. N. Y. Acad. Sci.* **192**, 25–43.
34. N. Stuhr-Hansen, T. I. Sølling, and L. Henriksen (2011). *Tetrahedron* **67**, 2633–2643.
35. Bruker Analytical X-ray Systems, *Smart & SAINT Software Reference Manuals, Version 6.45* (Bruker Analytical X-ray Systems, Madison, 2003).
36. G. M. Sheldrick, *SADABS an empirical absorption correction program* (Bruker Analytical X-ray Systems, Madison, 1996).
37. G. M. Sheldrick (2015). *Acta Crystallogr. Sect. C: Struct. Chem.* **71**, 3–8.
38. M. Emami, K. A. Ślepokura, M. Trzebiatowska, N. Noshiranzadeh, and V. Kinzhybalo (2018). *CrystEngComm* **20**, 5209–5219.
39. D. Casanova, P. Alemany, J. M. Bofill, and S. Alvarez (2003). *Chem. Eur. J.* **9**, 1281–1295.
40. Y.-Y. Li, N. Ren, S.-M. He, S.-P. Wang, and J.-J. Zhang (2020). *Appl. Organometal. Chem.* **34**, e5418.
41. C.-W. Jin, Y. Wang, N. Ren, L.-N. Geng, and J.-J. Zhang (2016). *J. Chem. Thermodyn.* **103**, 181–188.
42. J.-Y. Zhao, N. Ren, and J.-J. Zhang (2021). *Thermochim. Acta* **699**, 178915.
43. G. B. Deacon, P. C. Junk, W. W. Lee, M. Forsyth, and J. Wang (2015). *New J. Chem.* **39**, 7688–7695.
44. L. Zhong, W.-B. Chen, X.-H. Li, Z.-J. OuYang, M. Yang, Y.-Q. Zhang, S. Gao, and W. Dong (2020). *Inorg. Chem.* **59**, 4414–4423.
45. X. Feng, J. Zhao, B. Liu, L. Wang, S. Ng, G. Zhang, J. Wang, X. Shi, and Y. Liu (2010). *Cryst. Growth Des.* **10**, 1399–1408.
46. L. Hua, F.-W. Zheng, H.-T. Chen, L. Wang, D.-J. Li, L. Yang, F.-J. Han, X.-Y. Duan, T.-T. Liu, and W.-X. Wang (2021). *Solid State Chem.* **303**, 122463.
47. J.-B. Peng, Y.-P. Ren, X.-J. Kong, L.-S. Long, R.-B. Huang, and L.-S. Zheng (2011). *CrystEngComm* **13**, 2084–2090.
48. Y. M. Litvinova, Y. M. Gayfulin, A. S. Bogomyakov, D. G. Samsonenko, and Y. V. Mironov (2017). *J. Clust. Sci.* **28**, 3103–3114.
49. S. Yu, Z. Chen, H. Hu, B. Li, Y. Liang, D. Liu, H. Zou, D. Yao, and F. Liang (2019). *Dalton Trans.* **48**, 16679–16686.
50. W. Zhang, S.-M. Xu, Z.-X. Zhu, J. Ru, Y.-Q. Zhang, and M.-X. Yao (2020). *New J. Chem.* **44**, 2083–2090.
51. C. Zhang, X. Ma, P. Cen, X. Jin, J. Yang, Y.-Q. Zhang, J. Ferrando-Soria, E. Pardo, and X. Liu (2020). *Dalton Trans.* **49**, 14123–14132.
52. S.-L. Zhang, S.-S. Li, S.-Y. Zeng, Y. Shi, D.-Q. Wang, and L. Chen (2020). *New J. Chem.* **44**, 2408–2413.
53. Y.-P. Hua, C.-L. Xue, W.-M. Zhang, Y. Liu, J.-L. Tian, and W.-M. Wang (2021). *J. Mol. Struct.* **1227**, 129510.
54. Y. Wang, Z. Yuan, Y. Guo, X. Ma, Z. Meng, J. Sha, and H. Zhang (2020). *Z. Anorg. Allg. Chem.* **646**, 1696–1701.
55. K. Zhang, D. Liu, V. Vieru, L. Hou, B. Cui, F.-S. Guo, L. F. Chibotaru, and Y.-Y. Wang (2017). *Dalton Trans.* **46**, 638–642.
56. D.-F. Wu, H.-Y. Shen, X.-Y. Chu, W.-J. Chang, L.-H. Zhao, Y.-Y. Duan, H.-H. Chen, J.-Z. Cui, and H.-L. Gao (2018). *New J. Chem.* **42**, 16836–16845.
57. C.-M. Liu, R. Sun, B.-W. Wang, F. Wu, X. Hao, and Z. Shen (2021). *Inorg. Chem.* **60**, 12039–12048.
58. J. Liu, Y.-C. Chen, J.-L. Liu, V. Vieru, L. Ungur, J.-H. Jia, L. F. Chibotaru, Y. Lan, W. Wernsdorfer, S. Gao, X.-M. Chen, and M.-L. Tong (2016). *J. Am. Chem. Soc.* **138**, 5441–5450.
59. C.-M. Liu, D.-Q. Zhang, J.-B. Su, Y.-Q. Zhang, and D.-B. Zhu (2018). *Inorg. Chem.* **57**, 11077–11086.
60. F. Zhang, R.-F. Zhang, J. Ru, J. Wang, Q.-L. Li, and C.-L. Ma (2021). *Z. Anorg. Allg. Chem.* **647**, 1213–1220.
61. X. Mi, D. Sheng, Y. E. Yu, Y. Wang, L. Zhao, J. Lu, Y. Li, D. Li, J. Dou, J. Duan, and S. Wang (2019). *ACS Appl. Mater. Interfaces* **11**, 7914–7926.
62. M. V. Marinho, D. O. Reis, W. X. C. Oliveira, L. F. Marques, H. O. Stumpf, M. Déniz, J. Pasán, C. Ruiz-Pérez, J. Cano, F. Lloret, and M. Julve (2017). *Inorg. Chem.* **56**, 2108–2123.
63. P. Lin, F. Jiang, M. Wu, and M. Hong (2018). *Inorg. Chem. Commun.* **93**, 29–32.
64. T. Fujii, K. Kodaira, O. Kawauchi, N. Tanaka, H. Yamashita, and M. Anpo (1997). *J. Phys. Chem.* **101**, 10631–10637.
65. A. de Bettencourt-Dias, P. S. Barber, S. Viswanathan, D. T. de Lill, A. Rollett, G. Ling, and S. Altun (2010). *Inorg. Chem.* **49**, 8848–8861.
66. Y.-B. Lu, X.-M. Jiang, S.-D. Zhu, Z.-Y. Du, C.-M. Liu, Y.-R. Xie, and L.-X. Liu (2016). *Inorg. Chem.* **55**, 3738–3749.
67. A. Arauzo, L. Gasque, S. Fuertes, C. Tenorio, S. Bernès, and E. Bartolomé (2020). *Dalton Trans.* **49**, 13671–13684.
68. M.-F. Wu, M.-S. Wang, S.-P. Guo, F.-K. Zheng, H.-F. Chen, X.-M. Jiang, G.-N. Liu, G.-C. Guo, and J.-S. Huang (2011). *Cryst. Growth Des.* **11**, 372–381.
69. W. Xu, C.-J. Zhang, H. Wang, and Y. Wang (2017). *J. Clust. Sci.* **28**, 2005–2015.
70. P. Kalita, P. Nayak, N. Ahmed, J. M. Herrera, K. Venkatasubbaiah, E. Colacio, and V. Chandrasekhar (2020). *Dalton Trans.* **49**, 15404–15416.